POLITECNICO DI TORINO
Repository ISTITUZIONALE

# Fault section localization for pole-to-ground faults within de-energized areas of DC distribution systems under network parameter uncertainty

*Original*
Fault section localization for pole-to-ground faults within de-energized areas of DC distribution systems under network parameter uncertainty / Wang, H., Li, S., Yu, H., Bian, J., Li, G., Pons, E., Huang, T.. - In: INTERNATIONAL JOURNAL OF ELECTRICAL POWER & ENERGY SYSTEMS. - ISSN 0142-0615. - 182:(2026). [10.1016/j.ijepes.2026.112252]

*Availability:*
This version is available at: 11583/3017545 since: 2026-11-04T21:12:13Z

*Publisher:*
Elsevier Ltd

*Published*
DOI:10.1016/j.ijepes.2026.112252

*Terms of use:*

This article is made available under terms and conditions as specified in the corresponding bibliographic description in the repository

*Publisher copyright*

(Article begins on next page)

18 November 2026

Electrical Power and Energy Systems 182 (2026) 112252

Contents lists available at ScienceDirect

International Journal of Electrical Power & Energy Systems

journal homepage: www.elsevier.com/locate/ijepes

# Fault section localization for pole-to-ground faults within de-energized areas of DC distribution systems under network parameter uncertainty

He Wang [a], Shiqiang Li [a,*], Huanan Yu [a], Jing Bian [a], Guoqing Li [a], Enrico Pons [b], Tao Huang [b]

[a] Key Laboratory of Modern Power System Simulation and Control & Renewable Energy Technology, Ministry of Education, Northeast Electric Power University, Jilin, 132012, China

[b] Department of Energy, Politecnico di Torino, Torino, Piemonte, 10129, Italy

ARTICLE INFO

*Keywords:*
DC distribution network
Pole-to-ground fault
De-energized area
Network parameter Uncertainty
Fault section localization

ABSTRACT

Due to limited fault-isolation capability, the initial protection action in DC distribution systems may de-energize a feeder-level or multi-section area containing multiple candidate components. Identifying the specific pole-to-ground (PTG) faulted section within such a de-energized area using recorded fault transients remains challenging under limited measurement coverage and network parameter uncertainty. By exploiting the localized dominant response characteristics of transient zero-mode current (TZMC) during the early stage of PTG faults, this paper proposes a fault section localization method through sparse recovery of the dominant nodal TZMC support. First, the propagation and attenuation characteristics of early-stage TZMC are analyzed to identify a frequency band in which the nodal TZMC responses exhibit localized sparsity. A sparse localization model is then formulated via the impedance mapping between nodal TZMC responses and limited transient zero-mode voltage (TZMV) measurements, accounting for parameter-induced structured mismatch. Furthermore, a topology-aware residual-discriminative matching pursuit (TRMP) algorithm is developed to improve support recovery and thereby enhance fault section localization under such mismatch. The proposed method is validated on a modified IEEE 33-node DC distribution network in PSCAD/EMTDC. Simulation results show that the proposed method can distinguish bus faults from line-section faults and achieves higher localization accuracy than the compared sparse reconstruction methods under varying fault resistances, measurement noise levels, and network parameter uncertainty. Specifically, under network parameter uncertainty, the proposed method achieves average localization accuracies of 96.80 % and 98.99 % for bus-fault and midpoint line-fault scenarios, respectively.

## 1. Introduction

Direct current (DC) distribution networks offer inherent advantages for the flexible integration of distributed generators (DGs), DC loads, and energy storage systems [1–3]. With the increasing penetration of power electronic converters and DGs, modern DC systems are evolving toward highly complex architectures with multi-terminal interconnections [4,5]. In practice, however, DC breakers are not always deployed at all candidate isolation points in DC distribution systems. Therefore, when a permanent pole-to-ground (PTG) fault occurs, the initial protection action often de-energizes multiple sections including the faulted one, rather than isolating the faulted section directly. After such an initial isolation action, identifying the specific faulted bus or line section within the de-energized area becomes essential for subsequent selective isolation, maintenance dispatch, network reconfiguration, and service restoration [6,7].

Existing methods for fault section localization within de-energized areas can be broadly classified into two categories based on the information used for localization: active interrogation methods and passive fault-response methods. Active interrogation methods inject probing signals into the de-energized area and identify the faulted section from the resulting responses [8,9]. In [8], an additional control strategy coordinated with a resonant branch was employed to inject detection signals, and the fault section was identified from single-terminal information, whereas [9] utilized a hybrid HVDC circuit breaker to inject diagnostic pulses and identified the faulted line based on the resulting transient responses. Although these methods are well suited to restoration-oriented applications, their practical implementation generally requires additional signal-injection hardware or temporary intervention in converter control.

* Corresponding author.
*E-mail address:* neepu_lsq@163.com (S. Li).

https://doi.org/10.1016/j.ijepes.2026.112252
Received 20 July 2026; Received in revised form 10 October 2026; Accepted 18 October 2026
Available online 21 October 2026
0142-0615/© 2026 The Authors. Published by Elsevier Ltd. This is an open access article under the CC BY-NC-ND license (http://creativecommons.org/licenses/by-nc-nd/4.0/).

Passive fault-response methods, in contrast, infer the faulted section from fault-induced transient data recorded before the initial isolation action. These methods mainly include traveling-wave-based and model-based approaches. Traveling-wave methods exploit high-frequency wavefront information and can provide fast and informative signatures for fault section localization [10,11]. However, they depend on the reliable observation of early wavefronts and often require synchronized double-ended measurements, particularly in branched networks. Model-based methods establish analytical relationships between fault sections and measured responses [12,13]. In [12], the fundamental-frequency components of post-fault voltages and currents were estimated using least squares and then used for fault section localization. However, the method required a 5 ms post-fault window, during which the estimated components may be affected by emergency fault-control actions. To avoid reliance on fundamental-frequency estimation, [13] used high-frequency transients within the first 2.5 ms after fault inception and identified the faulted line by comparing transient impedances at branch terminals. Nevertheless, its applicability depends on the observability of branch-end high-frequency responses, limiting its use under sparse measurement configurations.

To reduce the dependence on measurement coverage, recent model-based studies have introduced sparse reconstruction into fault section localization [14–17]. These methods recover sparse fault representations from limited measurements using an impedance-based sensing matrix and identify the faulted section from the reconstructed support. However, two issues remain. First, the selected fault-feature components must retain sufficient transient energy while exhibiting clear node-domain sparsity; otherwise, their support may not be reliably recovered. Second, network parameters often deviate from their nominal values due to modeling simplifications, aging effects, and operational variations [18]. In sparse-reconstruction-based localization, such deviations manifest as structured impedance-mapping mismatch and may lead to incorrect support identification.

To address these challenges, this paper proposes a limited-measurement-based PTG fault section localization method that identifies the specific faulted bus or line section within a de-energized area by recovering the dominant nodal transient zero-mode current (TZMC) support from recorded transient zero-mode voltage (TZMV) under network parameter uncertainty. The main contributions of this paper are summarized as follows:

1) A frequency-dependent TZMC propagation model is constructed to quantify its local attenuation along DC feeders, revealing the spatial dominance of fault-adjacent nodal responses and providing a physical basis for characteristic-band selection and dominant-support-based fault section localization.
2) An impedance-mapping-based sparse localization model is established to recover the dominant nodal TZMC support from limited TZMV measurements, with network parameter deviations characterized as structured model mismatch.
3) A topology-aware residual-discriminative matching pursuit (TRMP) algorithm is proposed to reduce mismatch-induced false support selection through topology-constrained neighbor expansion and residual-energy validation, thereby improving fault section localization.

The remainder of this paper is organized as follows. Section 2 presents the overall implementation framework of the proposed method. Section 3 analyzes the propagation and node-domain characteristics of TZMC and determines the characteristic frequency band. Section 4 characterizes the impedance-mapping mismatch caused by network parameter uncertainty, formulates the corresponding sparse localization model, and presents the proposed TRMP algorithm and fault-section decision criterion. Section 5 evaluates the localization performance, robustness, and computational efficiency of the proposed method through simulation studies. Finally, Section 6 concludes the paper.

## 2. Overall framework of the proposed method

Following a PTG fault, the pole-voltage transients are first recorded during the interval before the initial protection action. The initial protection action may de-energize a feeder-level or multi-section area. The proposed method then uses the previously recorded fault transients to determine the specific PTG-faulted bus or line section within the resulting de-energized area for subsequent selective isolation and restoration support.

As shown in Fig. 1, the localization procedure consists of three main stages. First, the previously recorded pole-voltage transients are transformed into TZMV signals, and their characteristic-band components are extracted as observations. Second, based on the localized sparsity of fault-induced TZMC within the selected characteristic band, an impedance-mapping-based sparse localization model is established, in which network parameter uncertainty is represented as a structured mismatch between the nominal and actual impedance mappings. In the third stage, the proposed TRMP algorithm is employed to recover the dominant nodal TZMC support. The faulted section is then determined according to the reconstructed support pattern. Under the single-PTG-fault assumption, a dominant single-node support is interpreted as a bus fault, whereas a dominant adjacent-node-pair support indicates a line-section fault. This structured representation is established for PTG fault section localization within the de-energized area formed after the initial protection action, while multiple simultaneous faults and bipolar short-circuit faults are beyond the scope of this study.

## 3. Transient fault characteristics of PTG faults

### 3.1. Transient characteristics of PTG faults

During the early capacitor-discharge stage of a PTG fault, the transient fault current is primarily governed by the discharge of MMC submodule capacitors, the DC-side capacitors of voltage-source converters (VSCs), and the DC-side capacitors of dual-active-bridge (DAB) converters [19–21]. The main fault-current contributors and their associated current paths are schematically illustrated in Fig. 2.

Accordingly, the fault current in this stage can be approximately expressed as:

$$i_f(t) \approx i_{MMC}(t) + i_{VSC}(t) + i_{DAB}(t) \tag{1}$$

where $i_{MMC}(t)$, $i_{VSC}(t)$, and $i_{DAB}(t)$ denote the dominant discharge-current components contributed by the MMC submodule capacitors, the DC-side capacitors of the VSCs and DAB converters, respectively.

As shown in Fig. 2, the faulted pole is directly affected by the grounding fault path, while the non-faulted pole may also exhibit coupled transient responses. Therefore, the pole-mode transformation is employed to separate the line-mode and zero-mode components:

$$S = \frac{\sqrt{2}}{2}\begin{bmatrix} 1 & 1 \\ -1 & 1 \end{bmatrix} \tag{2}$$

$$\begin{bmatrix} X_1 \\ X_0 \end{bmatrix} = S^{-1}\begin{bmatrix} X_P \\ X_N \end{bmatrix} = \frac{\sqrt{2}}{2}\begin{bmatrix} 1 & -1 \\ 1 & 1 \end{bmatrix}\begin{bmatrix} X_P \\ X_N \end{bmatrix} \tag{3}$$

where $X_P$ and $X_N$ represent the electrical quantities at the positive and negative poles, respectively, and $X_1$ and $X_0$ denote the line-mode and zero-mode components. Compared with PTP faults, which mainly excite the line-mode component, PTG faults produce a more pronounced zero-mode component. Therefore, TZMC is adopted for subsequent PTG fault analysis and localization [16,17].

As shown in Fig. 3, during the initial stage of a PTG fault with $R_f = 1\ \Omega$, the time-domain responses of TZMC exhibit oscillatory decay behavior, while the spectral energy is mainly concentrated in the low- and medium-frequency ranges. As the fault resistance increases, the dominant frequency components tend to shift toward lower frequencies

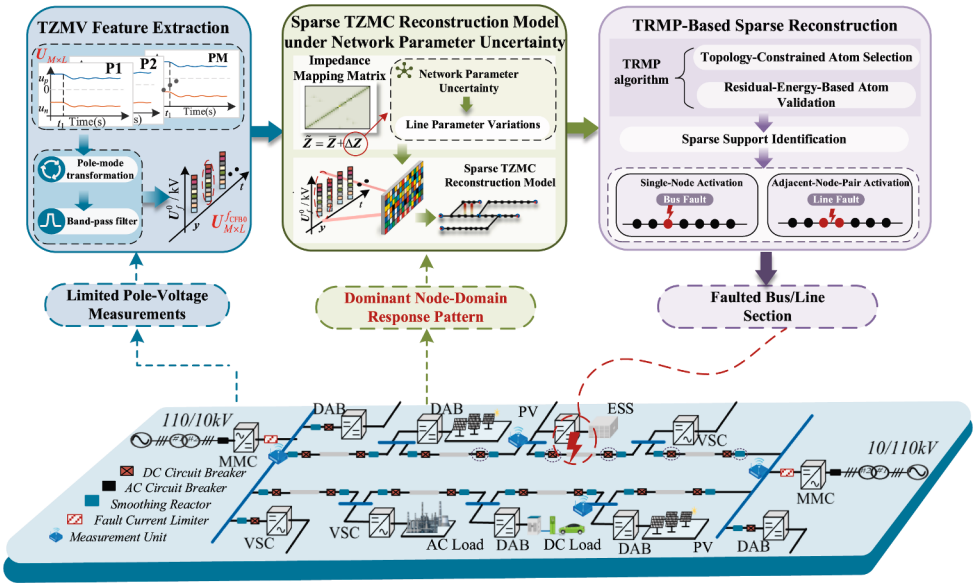



**Fig. 1.** Overall implementation framework of the proposed PTG fault section localization method under network parameter uncertainty.

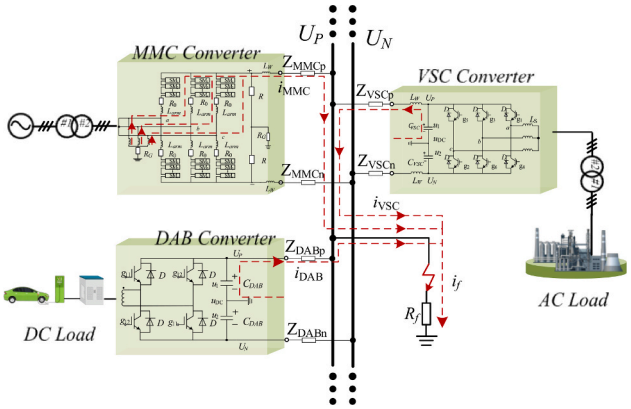



**Fig. 2.** Schematic of the main fault-current contributors and paths during the early capacitor-discharge stage.

because the equivalent discharge path becomes more resistive and the high-frequency transient components are further attenuated.

### 3.2. Propagation and node-domain characteristics of fault TZMC

During the early transient stage of a PTG fault in a multi-terminal DC distribution network, multiple converter-connected DC feeders simultaneously release capacitive discharge currents toward the fault point. To analyze the propagation and node-domain characteristics of TZMC, the fault point is modeled as an equivalent virtual current-injection node representing the aggregated fault-induced TZMC contributed by multiple converter-connected feeders, as illustrated in Fig. 4.

As illustrated in Fig. 4, during the early capacitor-discharge stage, the DC-side responses of VSC and DAB converters are mainly governed by their equivalent capacitances. Therefore, they are represented by a unified equivalent capacitive impedance:

$$Z_{cap} = \frac{1}{jwC_{cap}} \tag{4}$$

where $C_{cap}$ denotes the equivalent DC-side capacitance of the VSC/DAB converters. Unlike VSC and DAB converters, the MMC contains distributed submodule capacitors and arm inductances. Its discharge behavior is therefore represented by an equivalent RLC impedance:

$$Z_{MMC} = R_{eq} + jwL_{eq} + \frac{1}{jwC_{eq}} + R_g \tag{5}$$

where $R_{eq}$, $L_{eq}$ and $C_{eq}$ are the equivalent discharge parameters of the

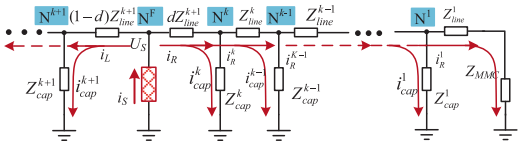


**Fig. 4.** Schematic illustration of fault-induced TZMC propagation during the early capacitor-discharge stage of a PTG fault.

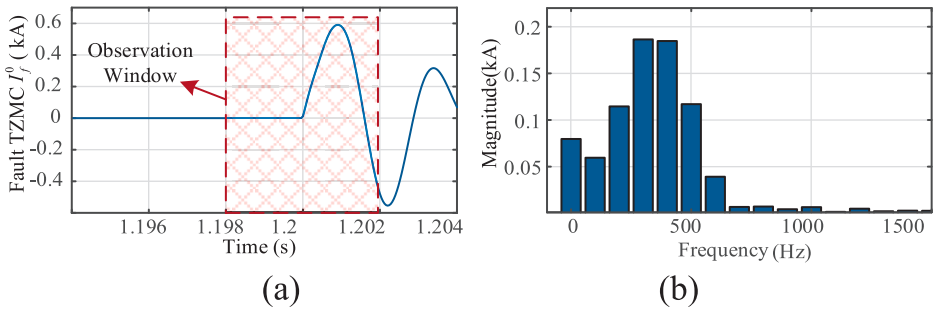



**Fig. 3.** Time- and frequency-domain characteristics of TZMC. (a) Time-domain characteristics. (b) Frequency-domain characteristics.

MMC, $R_{eq} = R_m/3$, $C_{eq} = 3C_0/N_1$, and $L_{eq}=(L_Z + L_m)/3$, $R_m$ represents the on-state resistance of the bridge arm switches, $C_0$ denotes the capacitance of the MMC sub-modules, $N_1$ is the number of sub-modules per phase, $L_m$ is the bridge arm inductance, and $L_Z$ is the equivalent inductance of the star reactor on the AC side of the MMC converter.

In Fig. 4, a PTG fault is assumed to occur between node $k$ and node $k + 1$, with $d \in [0, 1]$ denoting the normalized distance from the fault point to node $k$, the line impedance between adjacent nodes is denoted by $Z^k_{line}$. Let $Z^k_{eqr}$ denote the equivalent impedance seen from the downstream side of the k-th node, which can be recursively expressed as:

$$Z^k_{eqr} = \begin{cases} Z_{MMC} + Z^1_{line} & k = 1 \\ \left(Z^{k-1}_{eqr} \middle\| Z^{k-1}_{cap}\right) + Z^k_{line} & k > 1 \end{cases} \tag{6}$$

To characterize the propagation behavior of TZMC along the feeder, the local propagation ratio is defined as:

$$g_k(\omega) = \frac{i^k_R}{i^k_R + i^k_{cap}} = \frac{Z^k_{cap}}{Z^k_{cap} + Z^k_{eqr}} = \frac{1}{Z^k_{eqr}/Z^k_{cap} + 1} \tag{7}$$

where $g_k(\omega)$ represents the fraction of TZMC propagating through the $k$-th feeder section. Based on the parameter values listed in Appendix Tables A.1–A.3, the variation of $|g_k(\omega)|$ for typical feeder sections is shown in Fig. 5.

As shown in Fig. 5, the local propagation ratio $|g_k(\omega)|$ exhibits oscillatory behavior in the low-frequency region due to resonance and anti-resonance effects in the multi-branch RLC network, whereas a clearer attenuation trend appears in the medium- and high-frequency bands. Here, $k = 1$ corresponds to the boundary feeder section directly connected to the MMC equivalent impedance, whereas $k > 1$ represents recursively aggregated downstream sections. To highlight the propagation characteristics of typical internal feeder sections, only the cases with $k = 2$–5 are shown in Fig. 5.

Meanwhile, the time- and frequency-domain responses in Fig. 3 indicate that the main fault-induced transient energy is distributed mainly in the low- and medium-frequency ranges. In addition, Fig. 5 shows that the local propagation ratio presents a clearer attenuation trend in the medium-frequency range than in the low-frequency resonance region. Considering both transient energy concentration and local attenuation characteristics, the 200–400 Hz range is selected as the characteristic band in this study, which provides sufficient transient information while maintaining distinguishable node-domain responses for subsequent fault section localization. It should be noted that the selected band is used as a preset band-pass filtering range to obtain the corresponding band-limited time-domain component from the 4 ms fault-recording window for subsequent localization, rather than for high-resolution spectral estimation.

Within this band, TZMC responses are generally more significant at nodes close to the faulted section and gradually attenuate with propagation distance. This spatially nonuniform response provides the physical basis for identifying the dominant nodal support associated with the faulted section, although nonzero responses may still occur at other nodes owing to transient propagation. Accordingly, a dominant-response indicator for node $n$ can be conceptually represented as:

$$D^{f_{CFB0}}_n = \begin{cases} 0 I^{f_{CFB0}}_n < I^{f_{CFB0}}_{thre} \\ 1 I^{f_{CFB0}}_n \geqslant I^{f_{CFB0}}_{thre} \end{cases} \tag{8}$$

where $I^{f_{CFB0}}_n$ represents the peak magnitude of the TZMC within the characteristic frequency band at node $n$, and $I^{f_{CFB0}}_{thre}$ is a conceptual threshold for identifying relatively dominant characteristic-band TZMC responses. It should be noted that the nodal TZMC responses are not directly measured in practical applications; instead, their dominant support is inferred from limited TZMV measurements through the subsequent sparse localization model. The candidate dominant-response node set is therefore given by:

$$S_K = \left\{ n \middle| D^{f_{CFB_0}}_n = 1 \right\} \tag{9}$$

Under the single-PTG-fault assumption, the adopted localization representation uses a dominant single-node support centered on the faulted bus for a bus fault and a dominant two-node support associated with the adjacent terminal nodes of the faulted line section for a line fault. This representation is used for fault-section identification rather than as a strict upper bound on the number of nodes exhibiting TZMC responses.

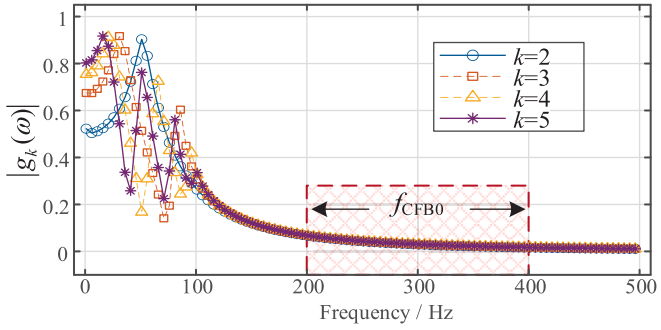



**Fig. 5.** Frequency-dependent local propagation ratio $|g_k(\omega)|$ along typical feeder sections ($k$ = 2–5).

## 4. Sparse fault section localization under network parameter uncertainty

### 4.1. Nominal impedance-based sparse localization model

According to the analysis in Section 3, the fault-induced TZMC responses exhibit a dominant node-domain response pattern within the selected characteristic frequency band. Within this band, the measured TZMV components and the nodal TZMC components satisfy

$$\boldsymbol{U}^{f_{CFB0}}_M = \overline{\boldsymbol{Z}}_{M\times N} \boldsymbol{I}^{f_{CFB0}}_N \tag{10}$$

where $\boldsymbol{U}^{f_{CFB0}}_M$ and $\boldsymbol{I}^{f_{CFB0}}_N$ denote the characteristic-band TZMV and nodal TZMC components, respectively, and $\overline{\boldsymbol{Z}}_{M\times N}$ is the nominal impedance mapping matrix from the $N$ nodal TZMC components to the TZMV components at the $M$ measurement points.

To identify the dominant nodal support rather than reconstruct phase-accurate transient waveforms, the magnitude of the nominal impedance mapping matrix is adopted to preserve the spatial response pattern required for support identification [14]. The discarded phase information and within-band impedance variations are treated as modeling errors in the reconstruction residual. Accordingly, the complex relationship in (10) is approximated over $L$ sampling instants as

$$\boldsymbol{U}^{f_{CFB0}}_{M\times L} \approx |\overline{\boldsymbol{Z}}_{M\times N}| \boldsymbol{I}^{f_{CFB0}}_{N\times L} \tag{11}$$

Here, $\boldsymbol{U}^{f_{CFB0}}_{M\times L}$ denotes the measured characteristic-band TZMV components, measured at $M$ measurement points over $L$ sampling instants within the complete 4-ms fault-recording window, and $I^{f_{CFB0}}_{N\times L}$ denotes the sparse nodal coefficient representation associated with the characteristic-band TZMC responses. Under ideal conditions, the dominant-support structure of $I^{f_{CFB0}}_{N\times L}$ enables reliable fault section localization via sparse reconstruction. Accordingly, the reconstructed coefficient matrix provides an equivalent representation of the dominant nodal TZMC support for localization, rather than a pointwise reconstruction of the physical TZMC waveform.

### 4.2. Fault section localization model under network parameter uncertainty

In practice, line parameters are subject to estimation errors, modeling simplifications, and operating variations. As a result, the actual line resistance and inductance between adjacent nodes deviate from their nominal values, which introduces perturbations into the admittance matrix and, consequently, into the impedance mapping used for localization. The perturbed resistance and inductance between nodes $i$ and $j$ can be expressed as:

$$\begin{cases} \widetilde{R}_{ij} = R_{ij}(1+\alpha_{ij}) \\ \widetilde{L}_{ij} = L_{ij}(1+\alpha_{ij}) \end{cases}, |\alpha_{ij}| < \delta \tag{12}$$

where $R_{ij}$ and $L_{ij}$ are nominal line parameters, $\alpha_{ij}$ denotes the relative perturbation coefficient, and $\delta$ represents parameter perturbation level. For simplicity, the same bounded perturbation coefficient is assigned to the resistance and inductance of the same line section to characterize line-parameter deviation. Accordingly, the perturbed admittance matrix is expressed as:

$$\widetilde{\boldsymbol{Y}} = \overline{\boldsymbol{Y}} + \Delta\boldsymbol{Y} \tag{13}$$

where $\overline{Y}$ denotes the nominal admittance matrix and $\Delta Y$ represents the perturbation induced by network parameter uncertainty. Under the small-perturbation assumption $\left\|\overline{\boldsymbol{Y}}^{-1}\Delta\boldsymbol{Y}\right\|_2 < 1$, first-order matrix perturbation theory yields

$$(\overline{\boldsymbol{Y}} + \Delta\boldsymbol{Y})^{-1} = \overline{\boldsymbol{Y}}^{-1} - \overline{\boldsymbol{Y}}^{-1}\Delta\boldsymbol{Y}\overline{\boldsymbol{Y}}^{-1} + O\left(\|\Delta\boldsymbol{Y}\|^2\right) \tag{14}$$

Accordingly, the perturbed full nodal impedance matrix can be approximated as

$$\widetilde{\boldsymbol{Z}}_{N\times N} \approx \overline{\boldsymbol{Z}}_{N\times N} - \overline{\boldsymbol{Z}}_{N\times N}\Delta\boldsymbol{Y}\overline{\boldsymbol{Z}}_{N\times N} \tag{15}$$

The rows associated with the $M$ measurement points form the impedance mapping used for fault localization. Therefore, the perturbed impedance mapping can be expressed as:

$$\widetilde{\boldsymbol{Z}}_{M\times N} = \overline{\boldsymbol{Z}}_{M\times N} + \Delta\boldsymbol{Z}_{M\times N} \tag{16}$$

where $\Delta Z_{M\times N}$ represents the topology-coupled perturbation in the impedance mapping induced by line-parameter deviations. Accordingly, the equivalent localization model based on the impedance-magnitude mapping can be expressed as:

$$\begin{cases} \boldsymbol{U}^{f_{\mathrm{CFB0}}}_{M\times L} \approx |\overline{\boldsymbol{Z}}_{M\times N}|\boldsymbol{I}^{f_{\mathrm{CFB0}}}_{N\times L} + \boldsymbol{\nu}_{M\times L} + \boldsymbol{e}_{M\times L} \\ \boldsymbol{\nu}_{M\times L} = \left(\left|\widetilde{\boldsymbol{Z}}_{M\times N}\right| - |\overline{\boldsymbol{Z}}_{M\times N}|\right)\boldsymbol{I}^{f_{\mathrm{CFB0}}}_{N\times L} \end{cases} \tag{17}$$

where $\boldsymbol{e}_{M\times L}$ denotes measurement noise and $\boldsymbol{\nu}_{M\times L}$ represents the equivalent structured disturbance induced by network parameter uncertainty.

In practical localization, only the nominal parameters are available, while the actual parameter perturbation level $\delta$ is unknown. Since the sparse nodal coefficients are estimated independently at each sampling instant, the sparse reconstruction problem for the $l$-th sample can be formulated as

$$\min\|\boldsymbol{I}^{f_{\mathrm{CFB0}}}_{l}\|_1 \quad \text{s.t.} \quad \left\|\boldsymbol{U}^{f_{\mathrm{CFB0}}}_{l} - |\overline{\boldsymbol{Z}}_{M\times N}|\boldsymbol{I}^{f_{\mathrm{CFB0}}}_{l}\right\|_2^2 \leqslant \eta \tag{18}$$

where $\eta$ bounds the squared residual energy induced by measurement noise and uncertainty-related model mismatch. Since the residual associated with the impedance-mapping mismatch also depends on the unknown TZMC responses, $\eta$ is difficult to specify a priori. Therefore, instead of directly solving (18) with a fixed global bound, the proposed TRMP evaluates each candidate neighboring atom according to its contribution to the reduction in residual energy.

### 4.3. Proposed TRMP reconstruction algorithm

To improve support identification under network parameter uncertainty, a TRMP algorithm is proposed. Compared with conventional greedy sparse reconstruction methods, the proposed algorithm improves support identification through two mechanisms.

1) Topology-aware support expansion: Instead of searching over all candidate nodes, the support search is restricted to physically connected nodes in the network graph. This topology-constrained expansion reduces the risk of selecting spurious supports caused by uncertainty-induced distortion in the impedance mapping.

2) Residual-discriminative atom validation: A residual-energy-based contribution criterion is introduced to evaluate whether a newly added atom leads to a meaningful reduction in the reconstruction residual. Unlike conventional greedy pursuit methods that update support purely according to correlation ranking, the proposed strategy uses the initial fault-induced response as a fixed reference to assess the effectiveness of newly introduced atoms, thereby improving support stability under structured model mismatch.

**Algorithm 1. TRMP Reconstruction Algorithm**

**Input:** sensing matrix $A = |\overline{Z}_{M\times N}|$, the observed matrix $\boldsymbol{y} = U^{f_{\mathrm{CFB0}}}_{M\times L_p}$ containing $L_p$ post-fault samples; the adjacency matrix $\boldsymbol{G}_{\boldsymbol{N}\times\boldsymbol{N}}$, the residual-contribution threshold $\gamma$.

**Output:** Reconstructed coefficient matrix $\widehat{\boldsymbol{\theta}}_{N\times L_p}$

1. Initialization: the initial post-fault sampling index as $l = 1$ with $l \in [1, L_p]$, and reconstruction coefficient matrix $\widehat{\boldsymbol{\theta}}_{N\times L_p} = \boldsymbol{0}_{N\times L_p}$
2. Iterative sparse reconstruction: For each sampling instant $l = 1, 2, \ldots, L_p$

1) Set iteration index $t = 1$, reference residual $\boldsymbol{r}^l_0 = \boldsymbol{y}_{:,l}$, $\overline{\boldsymbol{r}}^l_0 = \boldsymbol{r}^l_0$.

2) Compute the Pearson correlation coefficient.

$$\rho_i = \left|\mathrm{corr}(\boldsymbol{A}_i, \boldsymbol{r}^l_0)\right| \tag{19}$$

3) Select preliminary index $S_t = \underset{i}{\mathrm{argmax}}\rho_i$.

4) Construct the topology-constrained neighboring candidate set.

$$\boldsymbol{\Lambda}_t = \{m | \boldsymbol{G}(m, S_t) = 1, m \in [1, N]\} \tag{20}$$

$$\widetilde{S}_t = \underset{m\in\boldsymbol{\Lambda}_t}{\mathrm{argmax}}\rho_m \tag{21}$$

5) Determine the support set for the current iteration:

$$N_t = \begin{cases} \{S_1\} & t = 1 \\ \left\{S_1, \widetilde{S}_1\right\} & t = 2 \end{cases} \tag{22}$$

6) Estimate coefficients using initial reference residual:

$$\widehat{\boldsymbol{\theta}}^t_{N_t} = \underset{\boldsymbol{\theta}_{N_t}}{\mathrm{argmin}}\left\|\boldsymbol{r}^l_0 - \boldsymbol{A}_{N_t}\boldsymbol{\theta}_{N_t}\right\| = \left(\boldsymbol{A}^T_{N_t}\boldsymbol{A}_{N_t}\right)^{-1}\boldsymbol{A}^T_{N_t}\boldsymbol{r}^l_0 \tag{23}$$

7) Compute the residual of the current support set.

$$\widetilde{\boldsymbol{r}}_t = \boldsymbol{r}^l_0 - \boldsymbol{A}_{N_t}\widehat{\boldsymbol{\theta}}^t_{N_t} \tag{24}$$

8) Evaluate the residual-energy contribution of the current iteration.

$$c_t = \left(\|\widetilde{\boldsymbol{r}}_{t-1}\|_2^2 - \|\widetilde{\boldsymbol{r}}_t\|_2^2\right)/\|\boldsymbol{r}^l_0\|_2^2 \tag{25}$$

9) If $t < 2$, set $t = t + 1$, and return to step 5). Otherwise, evaluate the residual-energy contribution of the newly introduced atom. If $c_t < \gamma$, set $\widehat{\boldsymbol{\theta}}_{:,l} = \widehat{\boldsymbol{\theta}}^{t-1}_{N_{t-1}}$; otherwise, set $\widehat{\boldsymbol{\theta}}_{:,l} = \widehat{\boldsymbol{\theta}}^t_{N_t}$. Terminate the reconstruction at the current sampling instant.

Under the single-PTG-fault assumption, TRMP recovers the dominant structured support defined in Section 3 rather than the complete nodal TZMC response. A bus fault corresponds to a dominant single-node support, whereas a line-section fault corresponds to a dominant adjacent-node-pair support; therefore, the maximum support size is set to two, and responses propagated to other nodes are not treated as additional localization supports. The implementation steps are summarized in Algorithm 1. The reconstructed coefficient matrix $\widehat{\boldsymbol{\theta}}$ represents the estimate of the sparse nodal coefficient representation in (11) and (18). Accordingly, TRMP is a finite-step support-selection procedure that terminates after no more than two selection steps. Correct dominant-support recovery requires that (19) selects a true dominant atom as $S_1$; for a line-section fault, the other terminal node of the faulted line should subsequently be selected by (21) and retained according to Step 8 and Step 9, whereas, for a bus fault, the additional neighboring atom should be rejected by this criterion.

The residual-contribution threshold $\gamma$ controls the retention of the newly introduced neighboring atom. An excessively large $\gamma$ may reject the weaker but valid secondary support associated with the other terminal node of the faulted line section, whereas an excessively small value may retain spurious neighboring supports. Therefore, $\gamma$ should be selected as a relatively small positive threshold to avoid premature rejection of weak secondary supports. In this study, $\gamma = 0.02$ is used as the fixed setting, while occasionally retained spurious supports can be further screened based on the node activation ratio over the observation window.

### 4.4. Faulted-section decision based on node activation ratio

After obtaining the reconstructed coefficient matrix over the post-fault transient window, the node activation ratio is calculated to determine whether the reconstructed pattern corresponds to a bus fault or a line-section fault. Specifically, the activation ratio of node $i$ is defined as:

$$v_i = \left\|\widehat{\boldsymbol{\theta}}_{i,:}\right\|_0 \Big/ L_p \tag{26}$$

where $\widehat{\boldsymbol{\theta}}_{i,:}$ denotes the $i$-th row of $\widehat{\boldsymbol{\theta}}_{N\times L_p}$. Let $i_1 = \underset{i}{\operatorname{argmax}} v_i$, $i_2 = \underset{i\neq i_1}{\operatorname{argmax}} v_i$. If $G(i_1, i_2) = 1$ and $v(i_2) \geqslant \xi \cdot v(i_1)$, a line fault between nodes ($i_1$, $i_2$) is determined, otherwise, a bus fault at node $i_1$ is identified.

The physical basis of this criterion is related to the different nodal activation patterns caused by bus and line faults. For a bus fault, the transient response is mainly concentrated at the faulted node because the fault point directly corresponds to a single node, resulting in a single-node dominant pattern. In contrast, a line fault occurs between two adjacent nodes, and the transient response propagates toward both terminals of the faulted section, leading to effective support formation at two adjacent nodes. Therefore, the activation ratio provides an effective measure to identify whether a secondary node forms an effective support over the observation window, thereby distinguishing the single-node dominant pattern of bus faults from the dual-node support pattern of line faults.

Moreover, the fault-discrimination coefficient $\xi$ specifies the minimum relative activation ratio required for the secondary-node support. An excessively large $\xi$ may reject highly unbalanced two-node responses, particularly for near-terminal line faults, whereas an excessively small value may allow intermittent spurious activations to satisfy the criterion, thereby increasing false identification risks. Therefore, $\xi$ should be properly selected to retain weak but effective secondary supports while maintaining discrimination against spurious activations. In this study, $\xi = 0.1$ is used as the fixed setting.

## 5. Simulation and analysis

### 5.1. Test system and simulation settings

To validate the proposed method, simulations are conducted on a modified IEEE 33-node DC distribution network implemented in PSCAD/EMTDC, as shown in Fig. 6. The system includes MMC, VSC, and DAB converters, representing AC grid interfaces, DGs, and load interfaces, respectively. The network nodes are interconnected through DC feeders equipped with isolation switches, while DC circuit breakers are installed at MMC stations and DG access points. The detailed system parameters are given in Tables A.1–A.3 in the Appendix.

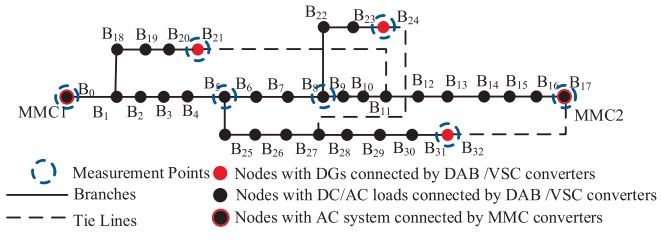



**Fig. 6.** Modified IEEE 33-node DC distribution network.

In Fig. 6, MMC1 operates in constant DC-voltage control mode, whereas MMC2 adopts constant active-power control. The VSC is controlled in AC-voltage regulation mode, and the DAB employs single-phase-shift control. The AC side of the MMC is grounded through a star-reactor grounding scheme with neutral-point resistance, while the DC side is grounded through a clamping resistor. The VSC and DAB units are grounded at the midpoint of their dc-link capacitors.

Based on the previous sparse-measurement localization studies in [14,16,17], seven measurement points are configured at $B_0$, $B_5$, $B_8$, $B_{17}$, $B_{21}$, $B_{24}$, and $B_{31}$. Specifically, $B_0$ and $B_{17}$ are located at the two MMC interfaces, $B_5$ and $B_8$ are located in the main feeder and major branching areas, and $B_{21}$, $B_{24}$, and $B_{31}$ cover different downstream branches and terminal sections. The measurements from different locations are required to be time-synchronized before constructing the TZMV response matrix, so that the transient responses at different measurement points correspond to the same sampling instants. The rows corresponding to these measurement nodes are extracted from the nodal impedance matrix $\boldsymbol{Z}_{NN}$ to form the sensing matrix $\boldsymbol{Z}_{MN}$ used for fault-section localization.

The sampling frequency is set to 25 kHz to provide sufficient temporal resolution for capturing transient dynamics. For each fault event, a 4 ms fault-recording window, including 2 ms before and 2 ms after fault inception, is adopted to capture the early capacitor-discharge-dominated transient stage before converter control responses and emergency fault-control actions significantly affect the network response. Based on the transient propagation analysis in Section 3, the 200–400 Hz range is selected as the characteristic band. The impedance mapping matrix is calculated at the center frequency of the selected band, i.e., 300 Hz, and used as the representative characteristic-band impedance mapping for sparse reconstruction, which is then used for subsequent fault section localization.

### 5.2. Localization performance under ideal conditions

Under ideal noise-free and nominal-parameter conditions, the correctness of the proposed sparse fault section localization model is first verified. Both positive PTG (PPTG) and negative PTG (NPTG) faults are simulated at all candidate nodes and at the midpoint of every line section, with fault resistance values ranging from 0.1 Ω to 200 Ω. For each fault-resistance setting, considering both fault polarities, 66 bus-fault cases and 64 midpoint line-fault cases are constructed based on the 33 candidate buses and 32 line sections, respectively. The overall localization results are summarized in Table 1.

As shown in Table 1, all bus-fault cases and midpoint line-fault cases are correctly localized over the tested fault-resistance range from 0.1 Ω to 200 Ω. This result verifies the basic feasibility of the proposed localization model and confirms that the characteristic-band TZMC responses can provide distinguishable dominant support patterns in the node domain under nominal conditions. For illustrative purposes, two PPTG faults with $R_f = 1$ Ω, one at node $B_{11}$ and the other on line $L_{10\text{–}11}$, are selected as representative bus-fault and line-fault cases, respectively, and the corresponding reconstructed support patterns are shown in Fig. 7.

As illustrated in Fig. 7(a), when a PPTG fault occurs at node B11, the reconstructed coefficient pattern is dominated by the faulted node, while the coefficients at other nodes remain relatively small. For the PPTG fault on line $L_{10\text{–}11}$ shown in Fig. 7(b), the two dominant reconstructed coefficients correspond to the adjacent terminal nodes $B_{10}$ and $B_{11}$. These results are consistent with the adopted localization representation, in which a bus fault is identified by a dominant single-node support, whereas a line-section fault is identified by a dominant

**Table 1**
Fault section localization results under different fault resistances.

| Fault type | Performance metrics | Fault resistance $R_f$ (Ω) | | | | | |
|---|---|---|---|---|---|---|---|
| | | 0.1 | 1 | 10 | 50 | 100 | 200 |
| Bus fault | Correct cases / total | 66/66 | 66/66 | 66/66 | 66/66 | 66/66 | 66/66 |
| | Location accuracy | 100 % | 100 % | 100 % | 100 % | 100 % | 100 % |
| Line fault | Correct cases / total | 64/64 | 64/64 | 64/64 | 64/64 | 64/64 | 64/64 |
| | Location accuracy | 100 % | 100 % | 100 % | 100 % | 100 % | 100 % |

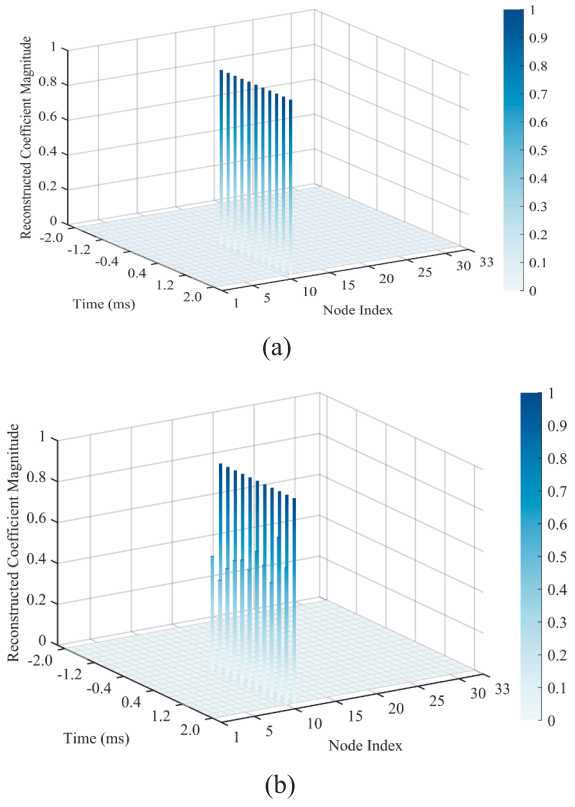



**Fig. 7.** Representative fault localization results under ideal conditions. (a) PPTG fault at node $B_{11}$. (b) PPTG fault on line $L_{10\text{-}11}$.

adjacent-node-pair support.

To further examine the physical consistency of the reconstructed support, Fig. 8 compares the temporal variations of the characteristic-band TZMC responses and the corresponding reconstructed coefficients for the same representative fault cases. For trend comparison, both quantities are normalized by their respective maximum absolute values.

For the bus fault at $B_{11}$, the reconstructed coefficient at $B_{11}$ exhibits a temporal variation consistent with the main response trend of the filtered TZMC at the same node. For the line fault on $L_{10\text{–}11}$, similar trend-level correspondence is observed at both terminal nodes $B_{10}$ and $B_{11}$. These results provide additional qualitative evidence that the reconstructed single-node and adjacent-node-pair supports are consistent with the characteristic-band TZMC responses.

### 5.3. Robustness under network parameter uncertainty

To emulate practical network-parameter deviations caused by parameter-estimation errors and incomplete asset records, relative perturbations are introduced into the line parameters. The parameter perturbation level is set to $\delta = 0$, 0.05, 0.10, and 0.15, and the corresponding relative line-parameter perturbations are randomly generated

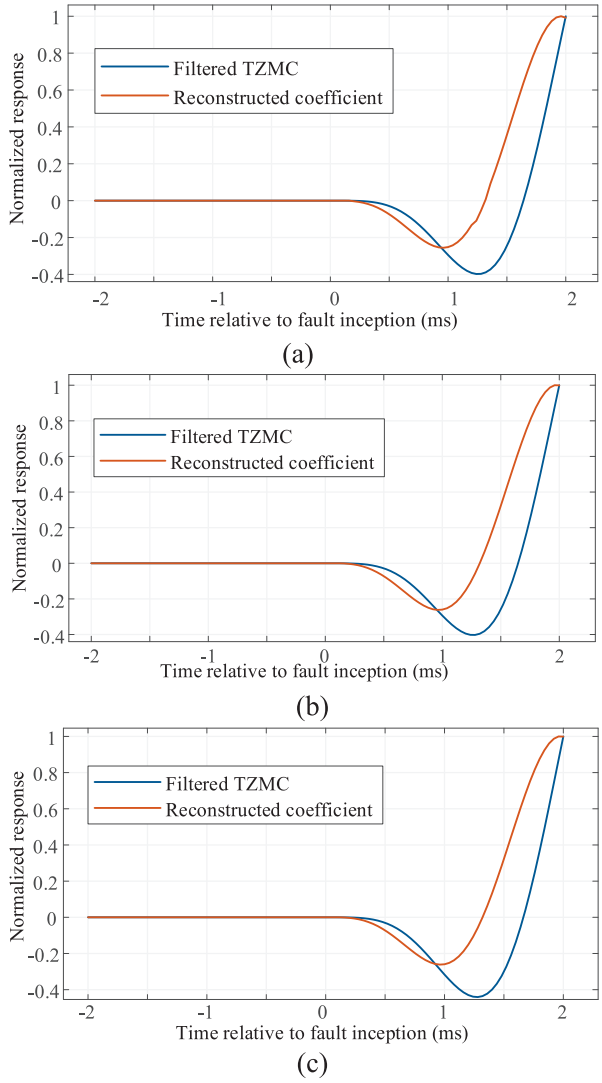



**Fig. 8.** Representative temporal comparisons between filtered TZMC responses and reconstructed coefficients under ideal conditions. (a) Node $B_{11}$ for the bus fault at $B_{11}$. (b) Node $B_{10}$ for the line fault on $L_{10\text{–}11}$. (c) Node $B_{11}$ for the line fault on $L_{10\text{–}11}$.

within $[-\delta, \delta]$. Under these conditions, a PPTG fault with $R_f = 1\ \Omega$ is simulated at all candidate nodes and at the midpoint of every line section. For each fault location and each perturbation level, 100 independent line-parameter realizations are generated. The localization accuracy is first evaluated over these realizations and then averaged over all bus-fault or midpoint line-fault locations, respectively. The proposed TRMP method is compared with Bayesian compressed sensing (BCS) [14], compressive sampling matching pursuit (CoSaMP) [15], and generalized orthogonal matching pursuit (GOMP) [16], as shown in Fig. 9. For a fair comparison, all methods use identical measurement settings and the nominal impedance-based sensing matrix. The 4-ms

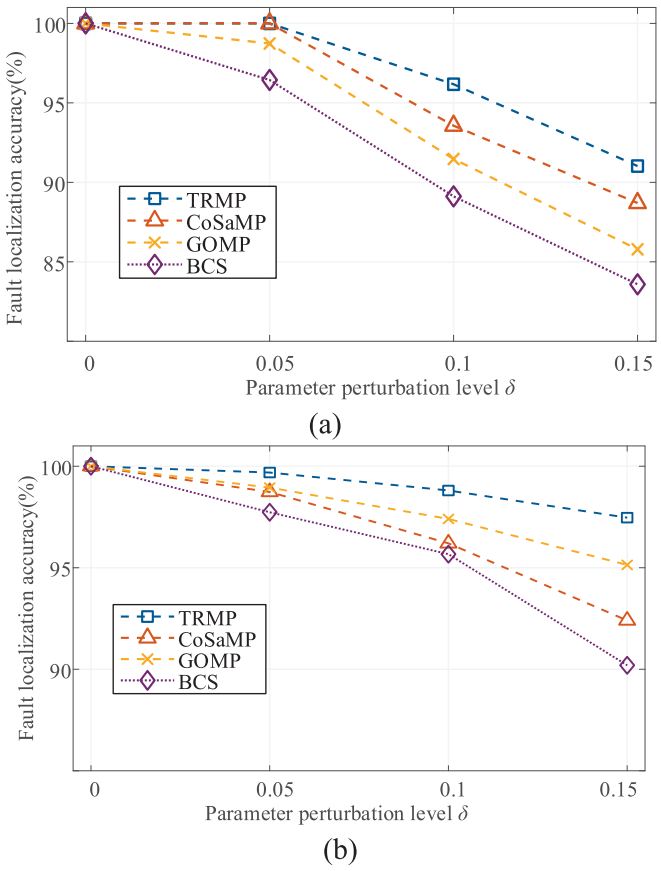



**Fig. 9.** Fault section localization accuracy of different algorithms under varying parameter perturbation levels. (a) Averaged results for all bus-fault cases. (b) Averaged results for all midpoint line-fault cases.

fault record is retained for signal processing, and only the 2-ms post-fault samples are used for sparse reconstruction. Since the faulted-section pattern is unknown before reconstruction, the sparsity level of CoSaMP and GOMP is fixed to 2 to cover both bus-fault and line-fault cases. It should be noted that the sparsity level determines the number of candidate supports retained during the reconstruction process. After reconstruction, dominant nodes are identified from the relative coefficient magnitudes, followed by the node-activation-ratio criterion in Section 4.4 for fault-section determination. All benchmark parameters are selected once and kept fixed throughout the experiments without case-by-case retuning.

As shown in Fig. 9(a), for the bus-fault scenario, the effect of network-parameter mismatch becomes more pronounced as the parameter perturbation level increases, resulting in a gradual decrease in localization accuracy for all methods. Nevertheless, the proposed TRMP method consistently achieves the highest localization accuracy over the entire perturbation range. This advantage is mainly attributed to the topology-aware support search and the residual-based atom discrimination mechanism, which jointly mitigate incorrect support selection under structured model mismatch. Averaged over all perturbation levels, TRMP achieves an average localization accuracy of 96.80 % for bus-fault cases, which is higher than CoSaMP, GOMP, and BCS by relative gains of 1.29 %, 2.98 %, and 4.89 %, respectively. These results indicate that TRMP shows better relative robustness under parameter uncertainty, although the accuracy decreases as the parameter perturbation level increases.

Similar observations can be made in the line-fault scenario shown in Fig. 9(b). Although all methods experience performance degradation as the parameter uncertainty increases, the proposed method achieves the highest average fault section localization accuracy among the compared algorithms. Averaged over all perturbation levels, TRMP achieves an average localization accuracy of 98.99 % for midpoint line-fault cases, yielding relative accuracy gains of 2.23 %, 1.14 %, and 3.22 % over CoSaMP, GOMP, and BCS, respectively.

### 5.4. Ablation analysis of the TRMP components

To evaluate the contributions of the two key components of TRMP, two ablated variants are constructed. The residual-based matching pursuit (RMP) removes the topology constraint while retaining the residual-contribution criterion, whereas the topology-constrained matching pursuit (TMP) retains the topology constraint but removes the residual-contribution criterion. Except for the removed component, all other procedures and settings follow Section 5.3. The average localization accuracies are evaluated separately for all bus faults and all midpoint line faults, and the corresponding ablation results are shown in Fig. 10.

As shown in Fig. 10(a), all three methods achieve perfect localization under nominal parameters. As the parameter perturbation level increases, the localization performance of RMP and TMP degrades more noticeably, whereas TRMP maintains relatively high accuracy. Averaged over all perturbation levels, TRMP achieves relative accuracy gains of 3.58 % and 3.09 % over RMP and TMP, respectively. These results indicate that both the topology constraint and residual-contribution criterion contribute to improving bus-fault localization under parameter mismatch.

For the midpoint line-fault cases shown in Fig. 10(b), TRMP consistently achieves higher localization accuracy than both ablated variants over the tested perturbation levels. Averaged over all perturbation levels, TRMP achieves relative accuracy gains of 7.30 % and 3.80 % over

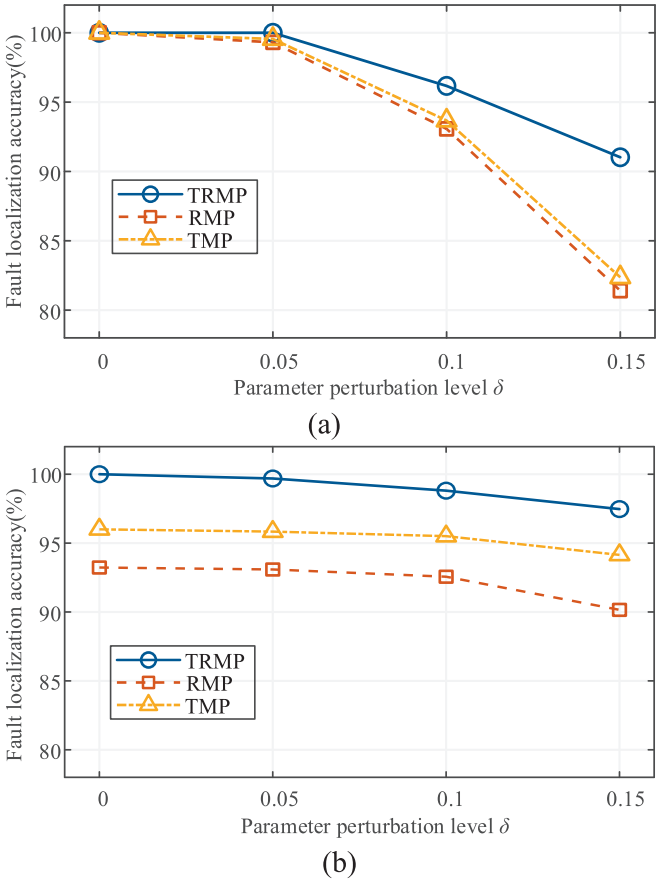



**Fig. 10.** Ablation results under line-parameter perturbations: (a) bus faults; (b) midpoint line faults.

RMP and TMP, respectively. These results further confirm the contributions of both components to line-fault localization. Under the tested midpoint line-fault conditions, the larger performance degradation of RMP indicates that the topology constraint provides the more pronounced contribution by restricting support recovery to physically feasible adjacent-node combinations, while the residual-contribution criterion provides further improvement in support reliability.

### 5.5. Influence of representative frequency on fault section localization

To assess the influence of the representative frequency, the test settings in Section 5.3 are retained, while the impedance-magnitude mapping matrix is recalculated at 200, 250, 300, 350, and 400 Hz. The resulting matrices are applied to the same bus-fault and midpoint line-fault cases under parameter-perturbation levels of $\delta = 0$, 0.05, 0.10, and 0.15. The comparison results are shown in Fig. 11.

As shown in Fig. 11, the localization performance exhibits a certain dependence on the representative frequency, particularly under stronger parameter perturbations. For both bus-fault and midpoint line-fault cases, the localization accuracy generally increases from the lower band edge toward 300 Hz and then decreases toward the upper band edge. Among the tested frequencies, the 300 Hz mapping consistently achieves the highest localization accuracy under all considered parameter-perturbation levels. Averaged over all perturbation levels, the 300 Hz mapping achieves localization accuracies of 96.80 % and 98.99 % for bus faults and midpoint line faults, respectively. These results support the use of 300 Hz as the representative frequency for the selected 200–400 Hz band.

### 5.6. Robustness under measurement noise

The robustness of the proposed method against measurement noise is further assessed under different signal-to-noise ratio (SNR) levels from 10 dB to 50 dB. A PPTG fault with $R_f = 1\ \Omega$ is simulated at all candidate nodes and at the midpoint of every line section, respectively. For each SNR level, independent Gaussian white noise is injected into the measured TZMV signals. In this study, the SNR is defined based on the TZMV signal before noise injection, and represents the power ratio between the original TZMV signal and the added Gaussian white noise. Each fault scenario is repeated 100 times with independent noise realizations, and the averaged localization accuracy is reported. The comparison results of the proposed method, CoSaMP, GOMP, and BCS are shown in Fig. 12.

As shown in Fig. 12(a), the localization accuracy of all methods improves as the SNR increases. The proposed TRMP method exhibits a clear advantage at relatively low SNR levels, while the performance differences gradually diminish as the SNR increases. Averaged over all tested SNR levels, the proposed method yields relative accuracy gains of 1.32 %, 3.54 %, and 2.33 % over CoSaMP, GOMP, and BCS, respectively.

A similar trend is observed in the midpoint line-fault scenario shown in Fig. 12(b). TRMP maintains better localization performance under relatively low SNR conditions, whereas the performance differences among the compared methods gradually decrease as the SNR increases. Averaged over all tested SNR levels, the proposed method yields relative accuracy gains of 3.15 %, 1.51 %, and 6.45 % over CoSaMP, GOMP, and BCS, respectively. Overall, the results demonstrate that the proposed method maintains better localization robustness against measurement noise, particularly under relatively low-SNR conditions.

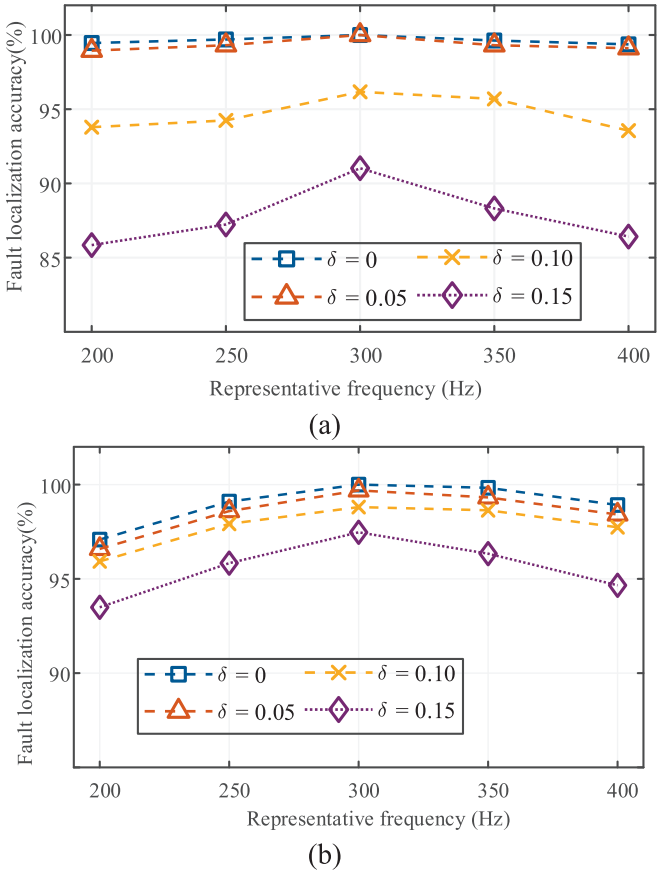



**Fig. 11.** Fault section localization accuracy under different representative frequencies and parameter perturbation levels. (a) Averaged results for all bus-fault cases. (b) Averaged results for all midpoint line-fault cases.

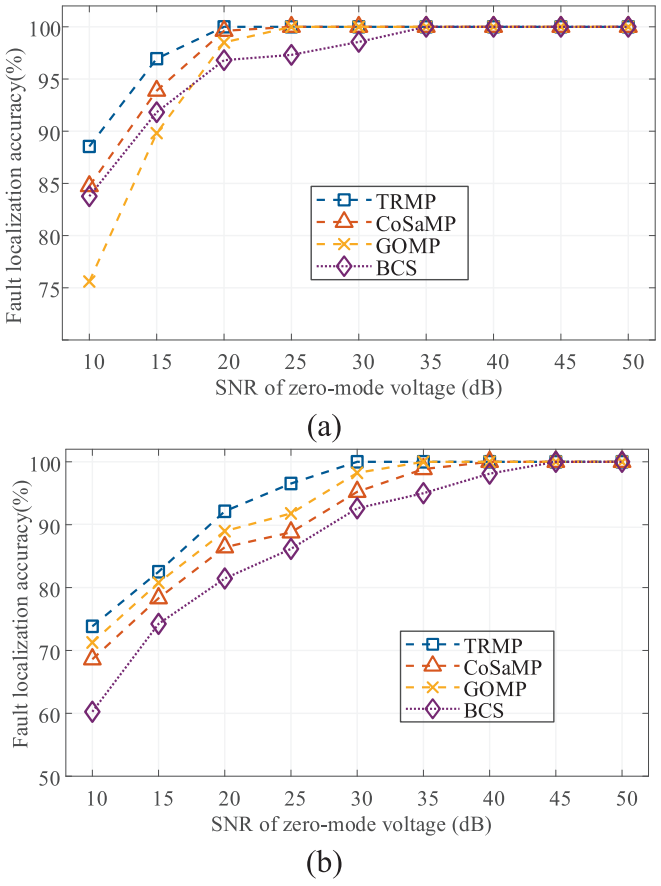



**Fig. 12.** Fault section localization accuracy of different reconstruction algorithms under varying SNR levels. (a) Averaged results for all bus-fault cases. (b) Averaged results for all midpoint line-fault cases.

### 5.7. Robustness under combined uncertainties

To further evaluate the robustness of the proposed method under combined uncertainties, a representative high-resistance PTG fault with $R_f = 100\ \Omega$ is simulated at bus $B_{11}$ and the midpoint of line $L_{10-11}$ ($d = 0.5$), respectively. Independent Gaussian white noise is injected into the measured TZMV signals, and the SNR is set to 20 dB. Meanwhile, different line-parameter perturbation levels ($\delta = 0$,0.05,0.10, and 0.15) are considered to emulate network parameter uncertainties. For each uncertainty condition, 100 independent realizations are generated, and the averaged localization accuracy is calculated. The comparison results of the proposed method and benchmark methods are shown in Fig. 13.

As shown in Fig. 13(a), under the high-resistance PTG fault condition with combined measurement noise and network parameter uncertainty, the localization accuracy of all methods decreases as the line-parameter perturbation level increases. The proposed TRMP method consistently achieves the highest localization accuracy among all compared methods. Averaged over all parameter perturbation levels, the proposed method achieves an average localization accuracy of 88.39 %, yielding relative accuracy gains of 4.01 %, 7.52 %, and 11.07 % over CoSaMP, GOMP, and BCS, respectively.

For the midpoint line-fault scenario shown in Fig. 13(b), TRMP also maintains better localization performance than the benchmark methods under all uncertainty levels. Averaged over all parameter perturbation levels, the proposed method achieves an average localization accuracy of 85.92 %, yielding relative accuracy gains of 3.00 %, 1.47 %, and 14.09 % over CoSaMP, GOMP, and BCS, respectively. Overall, the results demonstrate that the proposed TRMP method consistently outperforms the benchmark methods under combined measurement noise and network parameter uncertainty, indicating its stronger robustness for PTG fault section localization with different node activation patterns.

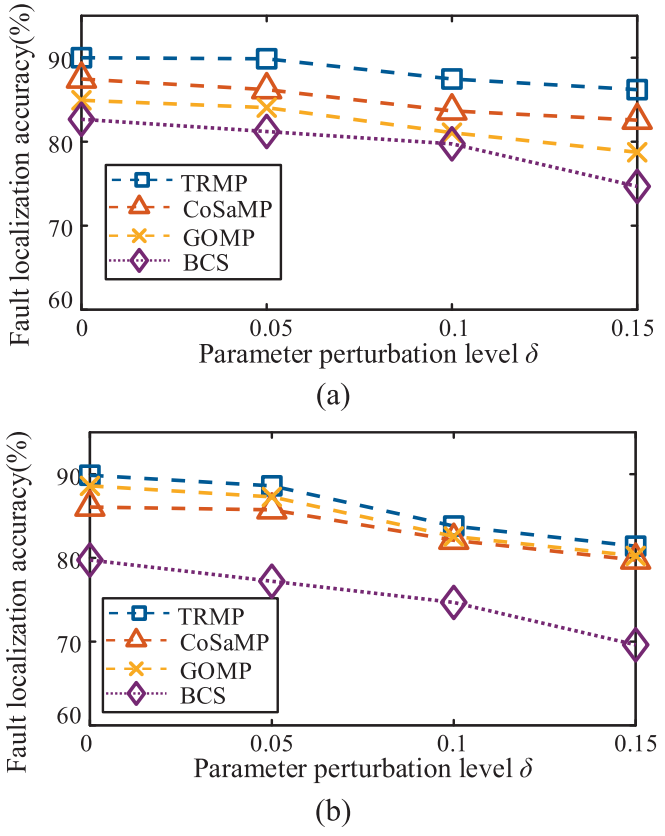



**Fig. 13.** Localization accuracy under combined measurement noise and network parameter uncertainty: (a) bus fault at $B_{11}$; (b) midpoint line fault on $L_{10-11}$.

### 5.8. Influence of fault-position coefficient on line-fault localization

#### 5.8.1. Network-wide localization performance at different fault positions

To further evaluate the applicability of the proposed method to different internal fault positions across the network, PTG faults are separately applied at multiple internal positions on each line section. For each line section, the fault-position coefficient $d$ is varied from 0.1 to 0.9 with a step of 0.1. The fault resistance is fixed at $R_f = 1\ \Omega$, and the line-parameter perturbation levels are set to $\delta = 0$, 0.05, 0.10, and 0.15. Under each perturbation level, 100 independent tests are performed using randomly generated parameter perturbations, and the network-wide average localization accuracy over all line sections is calculated. The results are shown in Fig. 14.

As shown in Fig. 14, the localization accuracy exhibits a consistent variation with the fault-position coefficient $d$ under different parameter-perturbation levels. As the fault moves from a near-terminal position toward the middle of the line, the localization accuracy gradually increases and reaches its highest level at around $d = 0.5$, and then decreases toward the opposite terminal. This behavior is mainly caused by the variation in the two-node support balance: near the line middle, both terminal-node responses are pronounced, whereas near a terminal, one response becomes dominant and the other weakens, reducing the distinguishability of the weaker support under limited measurements and parameter mismatch. Meanwhile, the increasingly dominant near-terminal response makes the two-node support pattern less distinguishable from the single-node-dominant pattern of an adjacent bus fault. Nevertheless, the weaker terminal response still contributes to support recovery, and TRMP can exploit topology-constrained support expansion and residual-contribution validation to maintain localization capability over the tested internal fault positions. Therefore, the observed position dependence mainly reflects the reduced distinguishability of the adjacent two-node support for near-terminal faults, while the proposed method remains applicable across the tested internal fault positions.

#### 5.8.2. Comparative localization performance at different fault positions

To further compare the localization performance of the considered algorithms under varying fault positions, line $L_{10-11}$ is taken as a representative line section. PTG faults with $R_f = 1\ \Omega$ are applied at $d = 0.2$, 0.4, 0.6 and 0.8, while the line-parameter perturbation levels are set to $\delta = 0$, 0.05, 0.10, and 0.15. The proposed method is compared with CoSaMP, GOMP, and BCS. Fig. 15 shows the localization accuracy of different methods under each fault-position coefficient, and Table 2 gives the averaged accuracy over different perturbation levels for each $d$.

As shown in Fig. 15 and Table 2, although all methods exhibit certain fault-position dependence, TRMP achieves the highest averaged

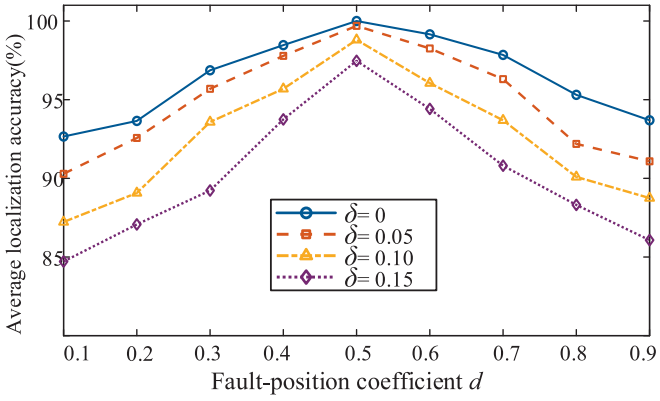



**Fig. 14.** Network-wide averaged localization accuracy under different fault-position coefficients and parameter-perturbation levels.

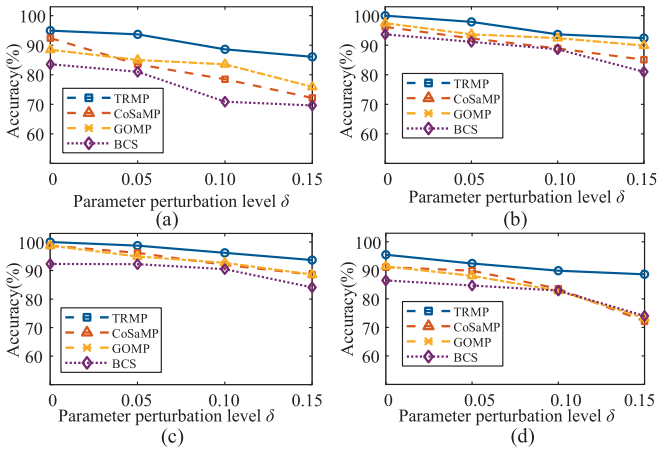



**Fig. 15.** Localization accuracy of different methods under different fault-position coefficients. (a) $d = 0.2$. (b) $d = 0.4$. (c) $d = 0.6$. (d) $d = 0.8$.

**Table 2**
Averaged localization accuracy under different fault-position coefficients.

| $d$ | TRMP | CoSaMP | GOMP | BCS |
|---|---|---|---|---|
| 0.2 | 90.82 % | 81.65 % | 83.23 % | 76.27 % |
| 0.4 | 95.99 % | 90.62 % | 93.35 % | 88.61 % |
| 0.6 | 97.15 % | 93.87 % | 93.75 % | 89.78 % |
| 0.8 | 91.59 % | 84.18 % | 83.89 % | 82.01 % |

localization accuracy at each tested position. Averaged over the four tested fault-position coefficients, TRMP yields relative accuracy gains of 7.20 %, 6.02 %, and 11.55 % over CoSaMP, GOMP, and BCS, respectively. These results indicate that TRMP provides better overall localization performance under varying fault positions and line-parameter mismatch, consistent with its topology-constrained support expansion and residual-contribution-based discrimination mechanisms.

### 5.9. Parameter validity analysis

To evaluate the validity of the selected parameters under different test conditions, four scenarios are constructed by considering measurement noise, line-parameter uncertainty, and fault position for bus and line faults. The detailed settings are summarized in Table 3. For each scenario, $\gamma$ is varied from 0.01 to 0.30 with an interval of 0.01, and $\xi$ is varied from 0.02 to 0.50 with an interval of 0.02. For each parameter combination, the average localization accuracy is calculated over all bus faults or all line faults corresponding to the considered scenario. The results for Scenarios 1–4 are shown in Fig. 16(a)–(d), respectively.

As shown in Fig. 16, the parameter sensitivity differs between bus and line faults. For the bus-fault cases in Scenarios 1 and 3, high localization accuracy is maintained over a broad range of $\gamma$ and $\xi$. In contrast, the line-fault cases in Scenarios 2 and 4 exhibit a narrower high-accuracy region, particularly under Scenario 4, where the near-terminal fault position, increased line-parameter uncertainty, and measurement noise jointly reduce the distinguishability of the secondary support. Nevertheless, the selected parameter pair ($\xi = 0.1, \gamma = 0.02$) remains within the high-accuracy region in all four scenarios. These results further verify the suitability of the fixed parameter setting ($\xi = 0.1, \gamma = 0.02$) under the considered test conditions.

**Table 3**
Test scenarios for parameter validity analysis.

| Scenario | Fault Type | $d$ | $\delta$ | SNR (dB) | $R_f$ (Ω) |
|---|---|---|---|---|---|
| 1 | Bus fault | – | 0.05 | 40 | 1 |
| 2 | Line fault | 0.5 | 0.05 | 40 | 1 |
| 3 | Bus fault | – | 0.15 | 20 | 1 |
| 4 | Line fault | 0.1 | 0.15 | 20 | 1 |

### 5.10. Computational efficiency analysis

To evaluate the computational efficiency of the sparse reconstruction stage, PPTG faults with $R_f = 1$ Ω are simulated at each candidate node and at the midpoint of every line section. Each experiment is repeated 100 times, and the average reconstruction time is recorded. All reconstruction algorithms are implemented under the same computing environment on a computer equipped with an Intel Core i7-8750 CPU and 16 GB RAM. The comparison results are shown in Fig. 17.

As illustrated in Fig. 17, the proposed TRMP method achieves an average reconstruction time of approximately 0.078 s per fault event, averaged over all simulated bus-fault and line-fault cases. Its runtime is lower than those of CoSaMP and GOMP, and moderately higher than that of BCS. Nevertheless, the proposed method maintains competitive computational efficiency while providing improved localization robustness under measurement noise and network parameter uncertainty.

It should be noted that the time reported in Fig. 17 only refers to the sparse reconstruction stage. It is used to evaluate the computational efficiency of different reconstruction algorithms rather than the complete fault localization procedure. Regarding scalability, the runtime of TRMP increases with network size as more candidate nodes are involved in support searching, while the topology-constrained secondary-support search and limited support size help restrict the additional computational burden. Overall, the obtained reconstruction time is acceptable for post-fault localization and restoration-support applications.

## 6. Conclusions and future work

This paper presented a limited-measurement-based method for locating PTG-faulted buses or line sections within de-energized areas of DC distribution systems. Within the selected characteristic frequency band, fault-induced TZMC responses exhibit spatial dominance near the faulted section, yielding dominant single-node and adjacent-node-pair supports for bus faults and line-section faults, respectively. Based on this property, a sparse localization model was formulated to represent impedance-mapping mismatch caused by line-parameter deviations. The proposed TRMP algorithm combines topology-constrained neighboring-node selection with residual-energy-based validation to improve support identification under such mismatch.

Simulations on a modified IEEE 33-node DC distribution network with seven voltage measurement points demonstrated the feasibility of the proposed method. Under nominal conditions, all tested PPTG and NPTG bus-fault and midpoint line-fault cases were correctly localized over the fault-resistance range of 0.1–200 Ω. In separate tests involving measurement noise and line-parameter perturbations, TRMP achieved the highest average localization accuracy among the compared sparse reconstruction methods. Its computational time is compatible with post-fault section localization and restoration-support applications rather than primary protection tripping.

The present study assumes a single PTG fault and uses a fixed measurement configuration in a simulation environment. Future work will investigate measurement-point placement for improved fault observability.

## CRediT authorship contribution statement

**He Wang:** Project administration, Methodology, Conceptualization. **Shiqiang Li:** Writing – original draft, Validation, Methodology, Investigation. **Huanan Yu:** Software, Formal analysis. **Jing Bian:** Methodology, Data curation. **Guoqing Li:** Methodology, Conceptualization. **Enrico Pons:** Writing – review & editing, Investigation. **Tao Huang:** Writing – review & editing, Methodology.

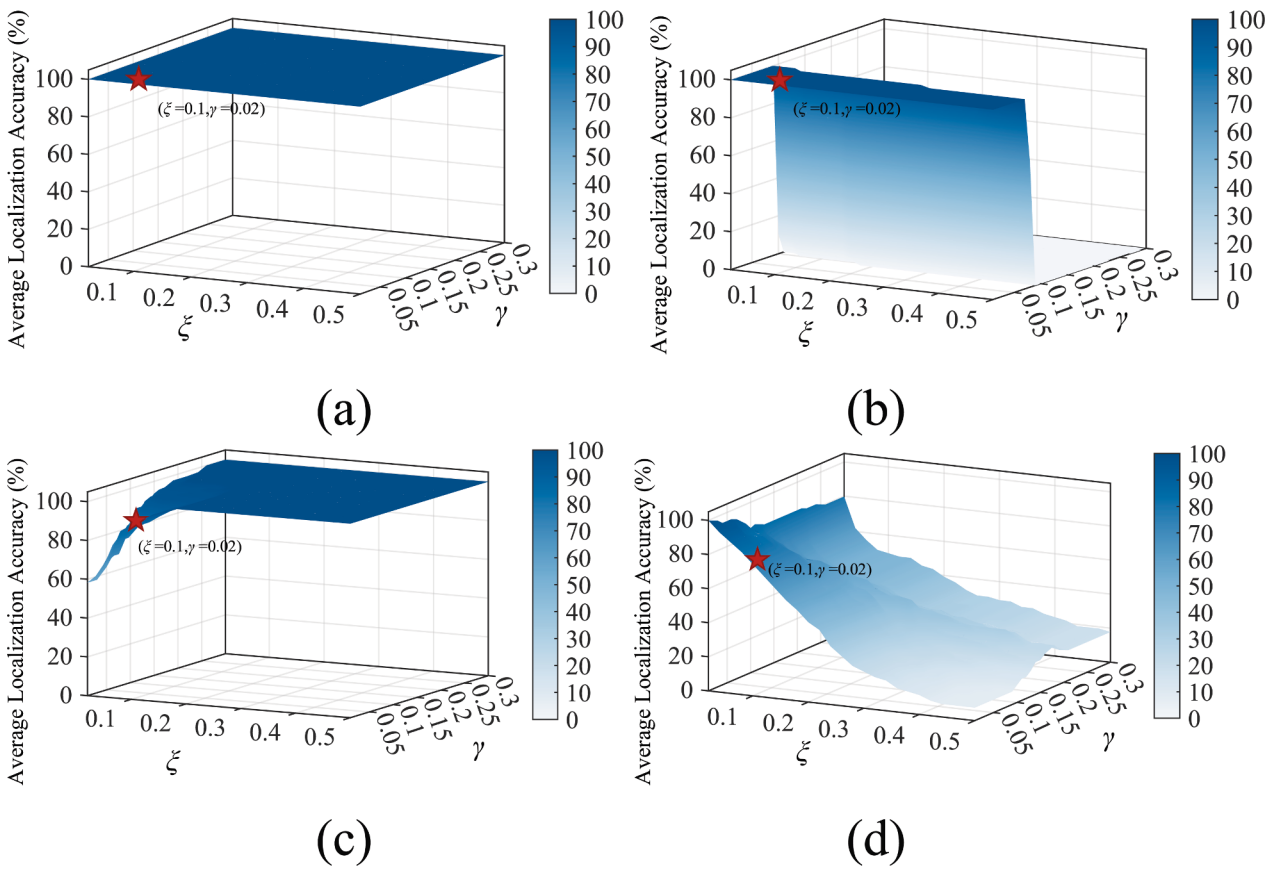



**Fig. 16.** Parameter validity under different test scenarios. The red marker denotes the selected parameter setting ($\xi = 0.1$, $\gamma = 0.02$). (a) Scenario 1; (b) Scenario 2; (c) Scenario 3; and (d) Scenario 4.

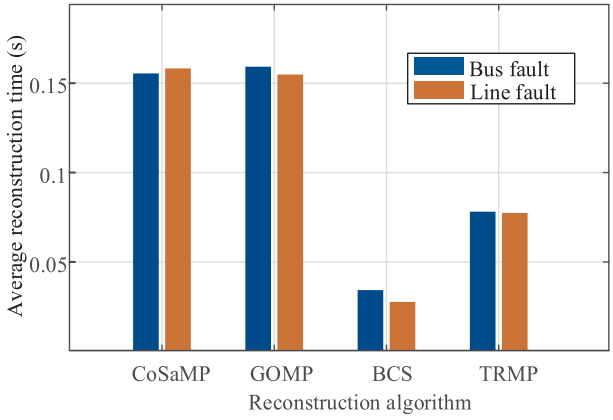



**Fig. 17.** Average reconstruction time of different reconstruction algorithms for bus-fault and line-fault cases.

## Declaration of competing interest

The authors declare that they have no known competing financial interests or personal relationships that could have appeared to influence the work reported in this paper.

## Acknowledgments

This work was supported by the National Science and Technology Major Project for Smart Grids under Grant 2025ZD0806800.

## Appendix

**Table A.1**
Detailed parameters of DC distribution network.

| System parameters | Value |
|---|---|
| Rated DC voltage (kV) | ±10 |
| Rated AC voltage (kV) | 10 |
| DC smoothing reactor (mH) | 2 |
| The resistance of DC line (Ω/km) | 0.0781 |
| The inductance of DC line (mH/km) | 0.8 |
| Length of DC line (km) | 10 |
| Grounding resistance (kΩ) | 1 |

**Table A.2**
Detailed parameters of converters.

| Converter parameters | Value |
|---|---|
| Rated Capacity of MMC (MVA) | 20 |
| Rated Capacity of VSC (MVA) | 5 |
| Rated Power of DAB (MW) | 3 |
| Bridge arm inductance of MMC (mH) | 20 |
| Submodule capacitance (μF) | 2000 |
| Number of MMC bridge arm sub-modules | 50 |
| Clamp resistors on the DC side of the MMC (Ω) | $10^6$ |
| DC-link capacitance of the VSC (μF) | 2000 |
| Number of VSC bridge arm sub-modules | 50 |
| High voltage side capacitance of the DAB (μF) | 1000 |

**Table A.3**
Load Parameters.

| Node | Load(MW) | Node | Load(MW) | Node | Load(MW) |
|---|---|---|---|---|---|
| 2 | 0.36 | 11 | 0.46 | 22 | 0.62 |
| 3 | 0.61 | 12 | 0.54 | 23 | 0.35 |
| 4 | 0.54 | 13 | 0.42 | 25 | 0.39 |
| 5 | 0.35 | 14 | 0.58 | 26 | 0.58 |
| 6 | 0.37 | 15 | 0.39 | 27 | 0.46 |
| 7 | 0.58 | 16 | 0.52 | 28 | 0.54 |
| 8 | 0.52 | 18 | 0.58 | 29 | 0.52 |
| 9 | 0.49 | 19 | 0.43 | 30 | 0.49 |
| 10 | 0.62 | 20 | 0.61 | 31 | 0.72 |

## Data availability

Data will be made available on request.

## References


[1] Raj Kamal Aluri V, Samantaray SR. An improved probe power unit (PPU)-based Fault location estimation in low-voltage DC microgrids. IEEE Trans Smart Grid 2024;15(6):5514–25.

[2] R Xu, Q Jiang, B Li, Y Liu, Y Zhu, Y Gu. Frequency-spectra impedance margin ratio for stability analysis of IBR-penetrated systems, IEEE Trans Power Syst, Early Access, pp. 1–16, Jun. 2026.

[3] Hassan SJU, Mehdi A, Haider Z, Song J-S, Abraham AD, Shin G-S, et al. Towards medium voltage hybrid AC/DC distribution systems: architectural topologies, planning and operation. Int J Electr Power Energy Syst 2024;159:110003.

[4] Zhu X, Zhou N, Liao J, Wang Q, Luo Y, Yu D. A multi-layer protection scheme for MMC-power electronic transformers. Int J Electr Power Energy Syst 2025;169:110786.

[5] Li D, Ukil A, Li G. Complex domain analysis-based fault detection in VSC interfaced multi-terminal DC system. IEEE Trans Ind Inf Jun. 2024;20(6):8306–16.

[6] Javed W, Chen D, Kucukdemiral I. Fault identifiability and pseudo-data-driven fault localization in a DC microgrid. Int J Electr Power Energy Syst 2023;148:108944.

[7] Liu L, Xie F, Kang X, Hao Z, Lekić A, Popov M. Parameter fitting-based traveling wave fault location method for multi-terminal DC grids. Int J Electr Power Energy Syst 2025;164:110412.

[8] Xu R, Song G, Chang Z, Zhang C, Yang J, Yang X. A ground fault section location method based on active detection approach for non-effectively grounded DC distribution networks. Int J Electr Power Energy Syst 2023;152:109174.

[9] Song G, Wang T, Hussain KST. DC line fault identification based on pulse injection from hybrid HVDC breaker. IEEE Trans Power Delivery Feb. 2019;34(1):271–80.

[10] Banafer M, Mohanty SR. Traveling wave-based primary protection and fault localization scheme for MTDC grid considering IEC 61869–9 measurement standard. IEEE Trans Instrum Measur 2023;72:1–16. 9002116.

[11] M Farshad, M Karimi. A signal segmentation approach to identify incident/reflected traveling waves for fault location in half-bridge MMC-HVdc grids, IEEE Trans Instrum Measur, 71, 1-9, 2022, Art no. 3501209.

[12] Panahi H, Sanaye-Pasand M, Niaki SHA, Zamani R. Fast low frequency fault location and section identification scheme for VSC-based multi-terminal HVDC systems. IEEE Trans Power Delivery Jun. 2022;37(3):2220–9.

[13] Jia K, Xuan Z, Feng T, Wang C, Bi T, Thomas DWP. Transient high-frequency impedance comparison-based protection for flexible DC distribution systems. IEEE Trans Smart Grid Jan. 2020;11(1):323–33.

[14] Jia K, Feng T, Zhao Q, Wang C, Bi T. High frequency transient sparse measurement-based fault location for complex DC distribution networks. IEEE Trans Smart Grid Jan. 2020;11(1):312–22.

[15] H Wang, D Wang, S Li, H Yu, J Bian, G Li. Fault section location method of DC distribution network based on multi-source fault information fusion, Int J Electr Power Energy Syst, 175, 111619, Feb. 2026.

[16] H Wang, Y Lu, S Li, H Yu, J Bian, A pole-to-ground fault location method for DC distribution network based on high-frequency zero-mode current sparsity, Electr Power Syst Res, 225, 109864, Dec. 2023.
[17] H Wang, Y Liu, S Li, H Yu, J Bian. Fault section location method for DC distribution networks based on sparse representation of current modal components, Measurement, 253, 117593, Sep. 2025.
[18] Mirshekali H, Dashti R, Shaker HR, Samsami R, Torabi AJ. Linear and nonlinear fault location in smart distribution network under line parameter uncertainty. IEEE Trans Ind Inf Dec. 2021;17(12):8308–18.
[19] Li B, Liao K, Yang J, He Z. Transient fault analysis method for VSC-based DC distribution networks with multi-DGs. IEEE Trans Ind Inf Nov. 2022;18(11):7628–38.
[20] Jiang S, Fan C, Huang N, Zhu Y, He M. A fault location method for DC lines connected with DAB terminal in power electronic transformer. IEEE Trans Power Delivery Feb. 2019;34(1):301–11.
[21] Dai Z, Liu X, He Y, Huang M. Single-terminal quantity based line protection for ring flexible DC distribution grids. IEEE Trans Power Deliv Feb. 2020;35(1):310–23.